International Journal of Nanomedicine

Dovepress
open access to scientific and medical research

Open Access Full Text Article

ORIGINAL RESEARCH

Multimodal Imaging-Guided Synergistic Photodynamic Therapy Using Carbonized Zn/Co Metal-Organic Framework Loaded with Cytotoxin Against Liver Cancer

Jingmei Huang[1,*], Lianshan Guo[1,*], Xiaoxiao Huang[1], Xiaoping Yu[2], Liqiao Lin[1], Xinlin Jiang[3], Zhihao Bai[4], Zhengzhao Li[1]

[1]Department of Emergency, The Second Affiliated Hospital of Guangxi Medical University, Nanning, Guangxi, 530007, People's Republic of China; [2]Department of Radiology, The Second Affiliated Hospital of Guangxi Medical University, Nanning, Guangxi, 530007, People's Republic of China; [3]Department of General Medicine, The Second Affiliated Hospital of Guangxi Medical University, Nanning, Guangxi, 530007, People's Republic of China; [4]College of Chemistry and Chemical Engineering, Guangxi University, Nanning, Guangxi, 530004, People's Republic of China

*These authors contributed equally to this work

Correspondence: Zhengzhao Li, Department of Emergency, The Second Affiliated Hospital of Guangxi Medical University, Nanning, Guangxi, 530007, People's Republic of China, Email lizhengzhao7680@163.com; Zhihao Bai, College of Chemistry and Chemical Engineering, Guangxi University, Nanning, Guangxi, 530004, People's Republic of China, Email zhihao_bai@163.com

Purpose: The study aimed to address the non-specific toxicity of cytotoxins (CTX) in liver cancer treatment and explore their combined application with the photosensitizer Ce6, co-loaded into carbonized Zn/Co bimetallic organic frameworks. The goal was to achieve controlled CTX release and synergistic photodynamic therapy, with a focus on evaluating anti-tumor activity against human liver cancer cell lines (Hep G2).

Methods: Purified cobra cytotoxin (CTX) and photosensitizer Ce6 were co-loaded into carbonized Zn/Co bimetallic organic frameworks, resulting in RGD-PDA@C-ZIF@(CTX+Ce6). The formulation was designed with surface-functionalization using polydopamine and tumor-penetrating peptide RGD. This approach aimed to facilitate controlled CTX release and enhance the synergistic effect of photodynamic therapy. The accumulation of RGD-PDA@C-ZIF@(CTX+Ce6) at tumor sites was achieved through RGD's active targeting and the enhanced permeability and retention (EPR) effect. In the acidic tumor microenvironment, the porous structure of the metal-organic framework disintegrated, releasing CTX and Ce6 into tumor cells.

Results: Experiments demonstrated that RGD-PDA@C-ZIF@(CTX+Ce6) nanoparticles, combined with near-infrared laser irradiation, exhibited optimal anti-tumor effects against human liver cancer cells. The formulation showcased heightened anti-tumor activity without discernible systemic toxicity.

Conclusion: The study underscores the potential of utilizing metal-organic frameworks as an efficient nanoplatform for co-loading cytotoxins and photodynamic therapy in liver cancer treatment. The developed formulation, RGD-PDA@C-ZIF@(CTX+Ce6), offers a promising avenue for advancing the clinical application of cytotoxins in oncology, providing a solid theoretical foundation for future research and development.

Keywords: metal-organic frameworks, cytotoxins, photodynamic therapy, liver cancer

Introduction

Liver cancer stands as one of the most prevalent and lethal malignancies globally. As per 2020 statistics, it ranks sixth worldwide, asserting its place among the most common cancer types and holds the third position in cancer-related mortality.[1] The carcinoma's highly invasive nature, coupled with an absence of early discernible symptoms, renders early diagnosis and intervention profoundly challenging. While conventional oncological treatments have seen some advancements, the therapeutic

Received: 26 December 2023
Accepted: 23 April 2024
Published: 11 May 2024

outcomes for liver cancer, hindered by tumor heterogeneity and drug resistance, remain suboptimal.[2,3] Thus, there's an urgent call to pioneer novel therapeutic strategies to enhance the survival rates and quality of life for patients afflicted with this condition.

Nanomedicine, as an emergent therapeutic strategy, has garnered considerable attention in the realm of oncology in recent years. The distinct properties of nanomaterials position them as promising vectors capable of concurrently ferrying multiple therapeutic agents, orchestrating a multifaceted assault on tumors.[4–6] The Zn/Co metal-organic frameworks represent a class of nanomaterials endowed with exceptional modularity and multifunctionality. Their expansive surface area and porous architecture offer an optimal platform for combinatorial drug therapy. These frameworks adeptly adsorb and accommodate various drug molecules, ensuring precise drug deployment within the acidic milieu of tumor environments.[7]

Cobratoxin (CTX) is an alkaline cationic polypeptide, isolated from cobra venom, spanning 60–63 amino acids and possessing a molecular weight between 6–7 Kda.[8] The anti-tumor mechanisms of CTX largely emanate from its role as a protein toxin, which can specifically bind to receptors on the cell membrane and subsequently infiltrate the cellular matrix. Once internalized, it exerts its lethal influence by disrupting intracellular protein synthesis and metabolic processes, culminating in cellular apoptosis and death.[9–11] Additionally, CTX instigates a cascade of cellular stress responses, such as intracellular oxidative stress, lipid peroxidation, and heightened calcium ion concentrations, thereby compromising the normal functions of tumor cells and inevitably leading to their demise.[12–14] Recognized for its potent anti-tumor potential, CTX is heralded as a significant candidate in oncological therapeutics. Yet, its non-specific cytotoxicity considerably curtails its clinical application.[15]

Photodynamic therapy (PDT) represents a burgeoning anti-tumor treatment modality predicated on the photoactivation of photosensitizers, leading to the generation of reactive oxygen species (ROS) and consequential tumor cell damage and demise.[16] Chlorin e6(Ce6), a photosensitizer routinely employed in PDT, is a chlorophyll-based compound, naturally existing as a biopigment in plants. Boasting pronounced photo-absorptive and photosensitive properties, when exposed to specific light wavelengths, Ce6 can absorb photon energy, transmuting it into highly reactive oxygen entities, such as singlet oxygen($^1O_2$).[17] These reactive oxygen derivatives, possessing potent oxidative potential, can inflict damage upon critical biomolecules like cell membranes, proteins, and nucleic acids, culminating in cell apoptosis and necrosis. PDT presents unique advantages in oncotherapy. Primarily, its capacity for localized treatment minimizes collateral damage to adjacent healthy tissue. Moreover, given the proclivity of photosensitizers to selectively accumulate in tumor tissue, PDT exhibits heightened specificity for tumors. Additionally, PDT can surmount resistance issues pervasive in conventional radiotherapy and chemotherapy, marking its potential as a transformative therapeutic tool.[18–20]

While cobratoxin (CTX) and photodynamic therapy (PDT) have demonstrated significant anti-tumor activity independently, singular therapeutic approaches often struggle with tumor heterogeneity. Multimodal imaging-guided therapeutic strategies, combined with the multifunctionality of nanomaterials, can enhance tumor interventions. Here, we introduce a novel nanoreactor that combines cytotoxin and photodynamic therapy to potentiate anti-tumor activity (Scheme 1). Specifically, we synthesized a magnetic carbonized Zn/Co-ZIF (C-ZIF) using a previous synthesis methodology,[21,22] and anchored CTX and the photosensitizer Ce6 onto C-ZIF, encased within polydopamine (PDA) to enhance biocompatibility. Subsequent condensation reactions adorned the ZIF's exterior with SH-RGD, culminating in the formation of the RGD-PDA@C-ZIF@(CTX+Ce6) nanoreactor (RPZC). The resulting nanoreactor (RPZC) not only attenuated CTX's hemolytic bioactivity but also preferentially accumulated at tumor sites, facilitated by RGD targeting and the Enhanced Permeation and Retention (EPR) effect. Within the acidic tumor microenvironment, RPZC released CTX and Ce6 into liver cancer cells, inducing apoptosis and generating singlet oxygen under 660nm laser irradiation, respectively. Meanwhile, the Co2+ within the nanoreactor catalyzes the transformation of hydrogen peroxide present in the tumor microenvironment into oxygen, augmenting the singlet oxygen concentration,[23] maximizing its PDT efficacy. Moreover, carbonized Zn/Co ZIF facilitated imaging diagnostics. Evaluating anti-tumor effects, the RPZC nanoreactor demonstrated superior in vivo anti-tumor activity, absent notable systemic toxicity. Our endeavors underscore the prodigious potential of employing metal-organic frameworks as drug delivery systems in multimodal imaging-guided combinatorial tumor therapy.

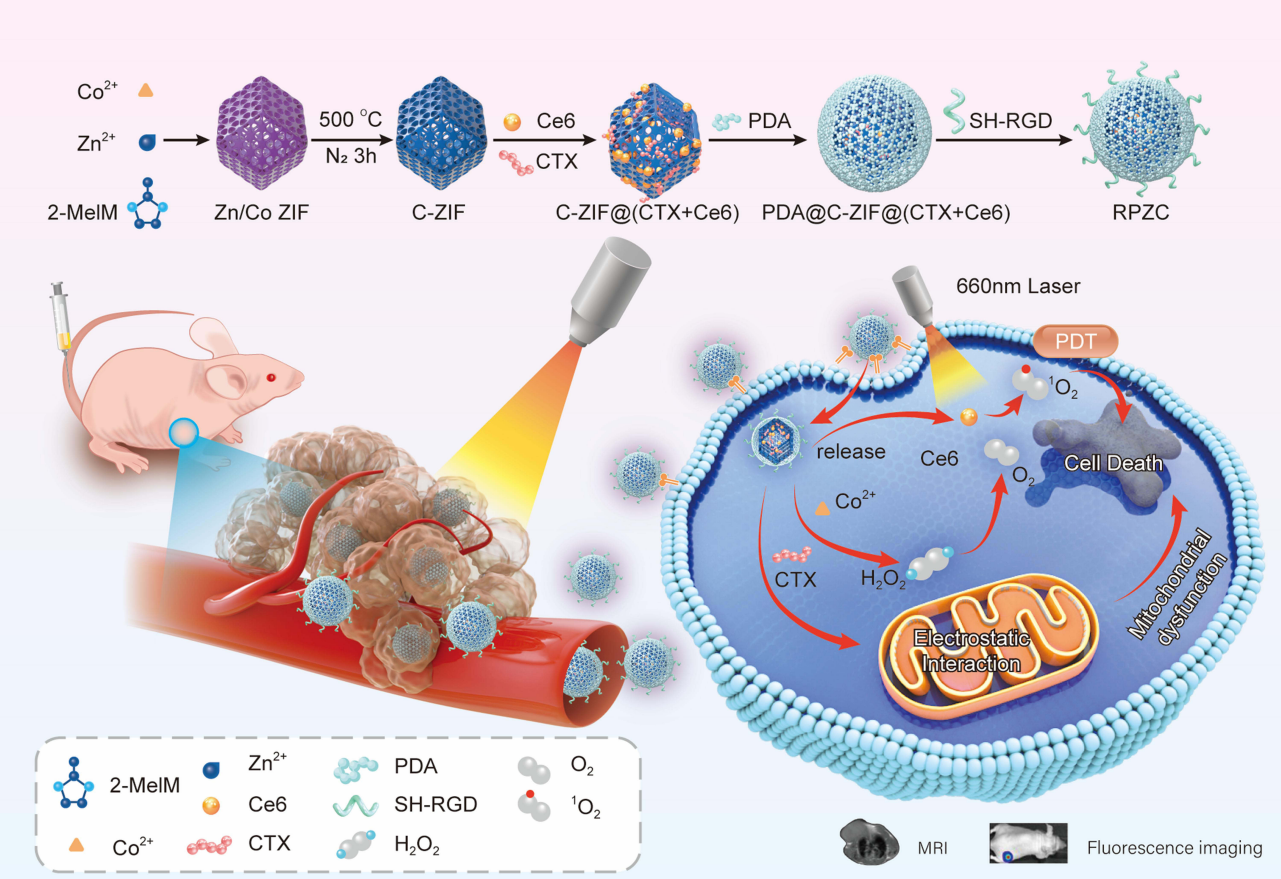

Scheme 1 Schematic of procedure of RPZC and therapeutic mechanism.

Materials and Methods

Materials

Zinc nitrate hexahydrate ($Zn(NO_3)_2{\cdot}6H_2O$), cobalt(II) nitrate hexahydrate ($Co(NO_3)_2{\cdot}6H_2O$), and 2-methylimidazole were procured from Sinopharm Chemical Reagent Co., Ltd. The cobra cytotoxin (CTX) was sourced from the Snake Venom Research Institute of Guangxi Medical University. Chlorin e6 (Ce6), SPDP, and SH-RGD were acquired from Xi'an Ruixi Biotechnology Co., Ltd. The Calcein/PI, JC-1 reagent test kit, Annexin V-FITC/PI apoptosis assay kit, and 2′,7′-dichlorofluorescin diacetate (DCFH-DA) were kindly supplied by Novozymes. Liver cancer cell lines (HepG2) and human normal liver cells (THLE-2) were obtained from the Chinese Academy of Medical Sciences, Beijing.

Synthesis of the RPZC

Preparation of Carbonized Zn/Co ZIF

Zinc nitrate hexahydrate (0.3633 g $Zn(NO_3)_2{\cdot}6H_2O$) and cobalt nitrate hexahydrate (0.3585 g $Co(NO_3)_2{\cdot}6H_2O$) were dissolved in 100 mL of methanol. Separately, 2-methylimidazole (1.6260 g) was also dissolved in 100 mL of methanol. This solution was then rapidly introduced into the prior mixture under vigorous stirring at room temperature. Upon combination, the solution transitioned from clear to a deep violet hue, indicating the onset of Zn/Co ZIF crystallization. After 12 hours of stirring, the solution was left undisturbed for 6 hours. The supernatant was then removed, and the precipitate underwent centrifugation at 10,000 rpm for 10 minutes, repeated thrice. The resultant Zn/Co ZIF was then subjected to carbonization at 500°C in a nitrogen atmosphere for 3 hours to yield carbonized Zn/Co ZIF (C-ZIF).

Loading of CTX and Ce6 Onto C-ZIF

Dissolving 4mg of CTX in ultrapure water, it was gradually added to the bare C-ZIF aqueous solution in a 1:1 mass ratio. Under ambient conditions, the mixture was magnetically stirred overnight. After centrifugation at 10,000 rpm for 10 minutes, the supernatant was discarded, and the C-ZIF@CTX nanoparticles were harvested. They were then rinsed twice with ultrapure water to eliminate any unbound CTX. The preparation methods for C-ZIF@Ce6 nanoparticles and C-ZIF@(CTX+Ce6) nanoparticles are analogous to the aforementioned procedure, with the exception that stirring was conducted in the absence of light.

Synthesis of the RGD-PDA@C-ZIF@(CTX+Ce6)

Dissolve 5mg of dopamine in 5mL of an aqueous solution containing Tris-HCl, adjusting the pH to 8.0–8.5. Subsequently, under stirring conditions, introduce it to the suspension of C-ZIF@(CTX+Ce6) nanoparticles. Allow it to stir for 4 hours at room temperature in the dark. To this solution, sequentially add 20μL of N-Succinimidyl 3-(2-pyridyldithio)-propionate (SPDP) and 5mg of SH-RGD. Through the NHS ester and pyridyl dithio reactive groups, a disulfide bond forms between the cysteine thiol, realizing the coupling of amine with thiol groups. Continue stirring for an additional 2 hours, centrifuge at 10,000rpm for 10 minutes, wash thrice with ultra-pure water, and lyophilize, storing at −20°C in the absence of light.

Characterization of Nanomaterials

Samples were characterized using a Scanning Electron Microscope (S-3400N, Zeiss, Germany), Particle Size/Zeta Potential Analyzer (Zetasizer Nano ZS90, Malvern Instruments, UK), X-ray Diffractometer (Bruker D8 Advance, Germany), Ultraviolet Spectroscopy (UV-2450PC), Fourier-Transform Infrared (FT-IR) Spectroscopy, X-ray Photoelectron Spectroscopy (XPS, Thermo Fisher Scientific 250Xi, USA), and Brunauer–Emmett–Teller (BET) analysis.

Oxygen Production

Under identical conditions, 3% hydrogen peroxide solution (100μL) was added to C-ZIF and RPZC solutions of varying concentrations (15, 30, 45, 60, 75, and 90μg/mL). The mixture was stirred at a steady, moderate pace, and the dissolved oxygen concentration was measured using a JPB-607A oxygen meter.

CTX Release

Dissolve 5 mg of RPZC in phosphate buffer solutions with pH values of 7.4, 5.5, and 4.5, respectively. Agitate on a temperature-controlled shaker set at 37°C. At specific intervals (0,5,1,2,4,6,8,12,24,36,48h), centrifuge to collect an aliquot of the supernatant while replenishing with an equivalent volume of PBS to the original solution. Quantify the CTX concentration in the supernatant over these intervals using the BCA protein assay method.

Quantification of Singlet Oxygen ($^1O_2$)

Under the illumination of a 660 nm laser, the capability of RPZC at various concentrations (5, 10, 20, 40, 80, 160, 320μg/mL) to generate singlet oxygen ($^1O_2$) in the presence of 100μL of 3% hydrogen peroxide was evaluated using the SOSG probe. Initially, RPZC samples of different concentrations were prepared, followed by the addition and blending of 100μL of 3% hydrogen peroxide, along with the introduction of the SOSG probe. The samples were then exposed to the 660 nm laser for 5 minutes, with the resultant singlet oxygen ($^1O_2$) production quantified through ultraviolet-visible absorption spectroscopy. Similarly, Electron Spin Resonance (ESR) was employed for the detection of $^1O_2$. Firstly, 100μL of 3% H^2O^2 was added to the RPZC solution (100μg/m L) containing the DMPO spin trap. ESR signals were then recorded under both dark and 660 nm laser irradiation for varying durations.

Hemolysis Assay

Fresh mouse whole blood was collected in anticoagulant tubes and centrifuged at 1000rpm for 5 minutes after thorough mixing. After washing thrice with PBS, the erythrocytes were resuspended in PBS to prepare a 2% red blood cell (RBC) suspension. A volume of 300μL RBC suspension was mixed with varying concentrations of free cobra cytotoxin and

RPZC. The negative control group consisted of RBC suspension mixed with PBS, while the positive control group had RBC suspension combined with deionized water. The samples were incubated at 37°C for one hour. Subsequently, they were centrifuged at 1000rpm for 15 minutes, aligned, and photographed. The absorbance of the supernatant from each group at 542nm was analyzed using a microplate reader.[24]

Cell Culture

HepG2 cells (human hepatocellular carcinoma cells) and THLE-2 cells (normal human liver cells) are cultured in DMEM medium (Gibco, USA) supplemented with 10% fetal bovine serum, maintained at 37°C in a 5% CO_2 incubator.

Analysis of RPZC Targeting and Uptake Capabilities

After inoculating 1×10^5 HepG2 and THLE-2 cells into culture dishes and incubating at 37°C in a 5% CO_2 environment for 24 hours, DMEM containing 100μg/mL RPZC was introduced for an additional 30 minutes. The dishes were subsequently rinsed with PBS, and cellular interactions were visualized using confocal laser scanning microscopy. HepG2 cells were further cultivated with DMEM supplemented with RPZC (100μg/mL) for varied durations (5min,30-min,1h,2h,4h), rinsed with PBS, and the red fluorescence of Ce6 was then observed under a fluorescence microscope.

Extracellular Generation of Reactive Oxygen Species (ROS)

To ascertain the intracellular ROS levels, the DCFH-DA probe was employed. Initially, 1×10^5 HepG2 cells were co-incubated with RPZC solution (100μg/mL) in a culture dish. Following a wash with PBS, a basic culture medium infused with DCFH-DA (1μM) was introduced and incubation continued for an additional 30 minutes. HepG2 cells were then exposed to a laser at a wavelength of 660nm and a power of 0.5W cm^{-2} for 5 minutes. Imaging was conducted utilizing a fluorescence microscope, and the intensity of the DCF fluorescence signal was measured to quantitatively determine the intracellular ROS levels.

Evaluation of Antitumor Effect in vitro

Utilizing the CCK-8 assay, we gauged the in vitro cytotoxic effects of the nanomaterial on cells. HepG2 cells were seeded at a density of 6000 cells per well in a 96-well plate and cultivated 12h at 37°C in a 5% CO_2 incubator, followed by a subsequent washing with PBS. A series of interventions were then performed on the cells at consistent concentrations but varying treatment types (control group: PBS, cells subjected to 660nm laser irradiation at a power of 0.5W/cm² for 5 minutes, C-ZIF: cells treated with bare carbonized ZIF, C-ZIF@Ce6: cells treated with C-ZIF@Ce6, C-ZIF@CTX: cells treated with C-ZIF@CTX, RPZC: cells treated with RPZC, RPZC+660nm Laser: cells treated with RPZC and subsequently irradiated with a 660 nm laser at 0.5W/cm² for 5 minutes). Subsequently, 10μL of CCK-8 solution was added to each well, with a further incubation of 2 hours. Absorbance at 450 nm was measured using a microplate reader, facilitating the calculation of cell viability and the median lethal dose. Similarly, the cytotoxicity of varying concentrations of RPZC under laser irradiation was assessed on normal liver cells (THLE-2).

The wound healing assay assesses the impact of various interventions on the cellular scratch wound healing process. HepG2 cells were cultivated in culture dishes until they reached optimal confluence. Thereafter, a fine-tipped tool was used to meticulously create a linear scratch across the cellular monolayer. Subsequently, the dish was gently rinsed with PBS to remove any detached cells and debris. Different types of cell culture mediums, as described in previous experimental groupings, were then introduced. Over designated time intervals (0,24h,48h), the progression of scratch closure was observed and documented. Real-time imaging was conducted under a microscope, capturing the cellular migration and the wound closure dynamics.

JC-1 staining is employed to examine mitochondrial membrane potential alterations in cells following various treatments. HepG2 cells were cultured in dishes at a density of 1×10^5 cells per dish and were subjected to interventions as previously described. Subsequently, JC-1 solution was introduced to the aforementioned dishes. After a continuation of incubation for 20 minutes, the dishes were rinsed with JC-1 buffer and imaged under a fluorescence microscope.

Calcein/PI staining is utilized to assess and analyze viable and non-viable cells. HepG2 cells, at a density of 1×10^5 cells per dish, were incubated in cell culture dishes for 24 hours and then subjected to the specified experimental

interventions as previously described. The Calcein/PI dye was introduced to the culture medium, and the cells were subsequently incubated at 37°C for 30 minutes. Following this, the dishes were rinsed with PBS and visualized under a fluorescence microscope.

The apoptosis rate of liver cancer cells is gauged using the Annexin V-FITC/PI assay kit. HepG2 cells were seeded in culture dishes at a density of 3×10^5 cells per well and incubated overnight. The culture medium was subsequently discarded, and the cells underwent treatment with PBS, L, C-ZIF, C-ZIF@Ce6, C-ZIF@Ce6+L, C-ZIF@CTX, RPZC, and RPZC+L (for the light-exposed groups, cells were illuminated under a laser with an excitation wavelength of 660nm and a power of 0.5W/cm^2 for 5 minutes). Following this, cells were digested, harvested, rinsed, and centrifuged. They were then stained according to the Annexin V-FITC/PI protocol, and the results analyzed via flow cytometry.

Establishment of the Tumor-Bearing Mouse Model

We established a subcutaneous HepG2 hepatocellular carcinoma model in nude mice to evaluate the in vivo therapeutic efficacy of RPZC. Experimental nude mice (BALB/c-nu, aged 4–5 weeks, evenly distributed between male and female) were procured from the Experimental Animal Center of Guangxi Medical University. All animal experiments were conducted under protocols approved by the Ethics Committee of the Second Affiliated Hospital of Guangxi Medical University (Approval Number: 2023-KY (0910)). A liver cancer model was established in each mouse by subcutaneously injecting 1×10^6 HepG2 cells.

Multimodal Imaging

Fluorescence imaging was executed using a small animal in vivo imaging system. RGD-PDA@C-ZIF@(CTX+Ce6) modified with RGD and the unmodified PDA@C-ZIF@(CTX+Ce6), were separately administered into tumor-bearing nude mice via tail vein injections at a dose of 200μL (100μg/mL). Following satisfactory anesthesia with a 1.25% Avertin (2,2,2-tribromoethanol) intraperitoneal injection, fluorescence signals within the tumor-bearing mice were chronicled at intervals post-injection: 0, 1, 4, 8, 12, 24, and 48 hours. Likewise, after intravenous administration of RGD-PDA@C-ZIF@(CTX+Ce6) NPs 200μL (100μg/mL) to the same cohort of tumor-bearing nude mice, magnetic resonance signal intensity at the tumor sites was assessed at distinct time points: 0, 2, 4, 6, 12, and 24 hours using magnetic resonance imaging.

Evaluation of Antitumor Effect in vivo

Tumor-bearing nude mice were methodically segregated into eight groups, each comprising five mice: G1: PBS; G2: Phototherapy; G3: C-ZIF; G4: C-ZIF@Ce6; G5: C-ZIF@Ce6+L; G6: C-ZIF@CTX; G7: RPZC; G8: RPZC+L. Treatment was initiated once tumor dimensions approximated 100mm^3. According to the designated groupings, varied nanomaterials 200μL (100μg/mL) were systematically administered into the mice via tail vein injections. For those groups necessitating laser irradiation, tumors were illuminated with a 660 nm laser (0.5Wcm^{-2}) for 5 minutes, precisely 4 hours post-injection. Every 24 hours, therapeutic intervention was executed, with tumor length (L) and width (W) every 48 hours measured using a caliper. This facilitated the calculation of tumor volume and the continual monitoring of weight variations in each mouse cohort. Upon the culmination of the treatment regimen, blood samples were procured, followed by the dissection of primary organs such as the heart, liver, spleen, lungs, and kidneys, along with tumor tissue, priming them for subsequent analytical assessments.

Statistical Analysis

All data are presented as mean ± standard deviation (SD). The statistical significance of differences between the two groups was assessed using *t*-tests, while comparisons among multiple groups were conducted using one-way analysis of variance. In all analyses, statistical significance is denoted as ns (not significant), $*p < 0.05$, $**p < 0.01$, $***p < 0.001$.

Results and Discussion

Characterization of Nanomaterials

Under scanning electron microscopy, the prepared C-ZIF exhibited a particulate distribution with excellent dispersion (Figure 1A(I–II)). Its average size measured approximately 93.24±2.14nm (Figure 1B). The Brunauer-Emmett-Teller

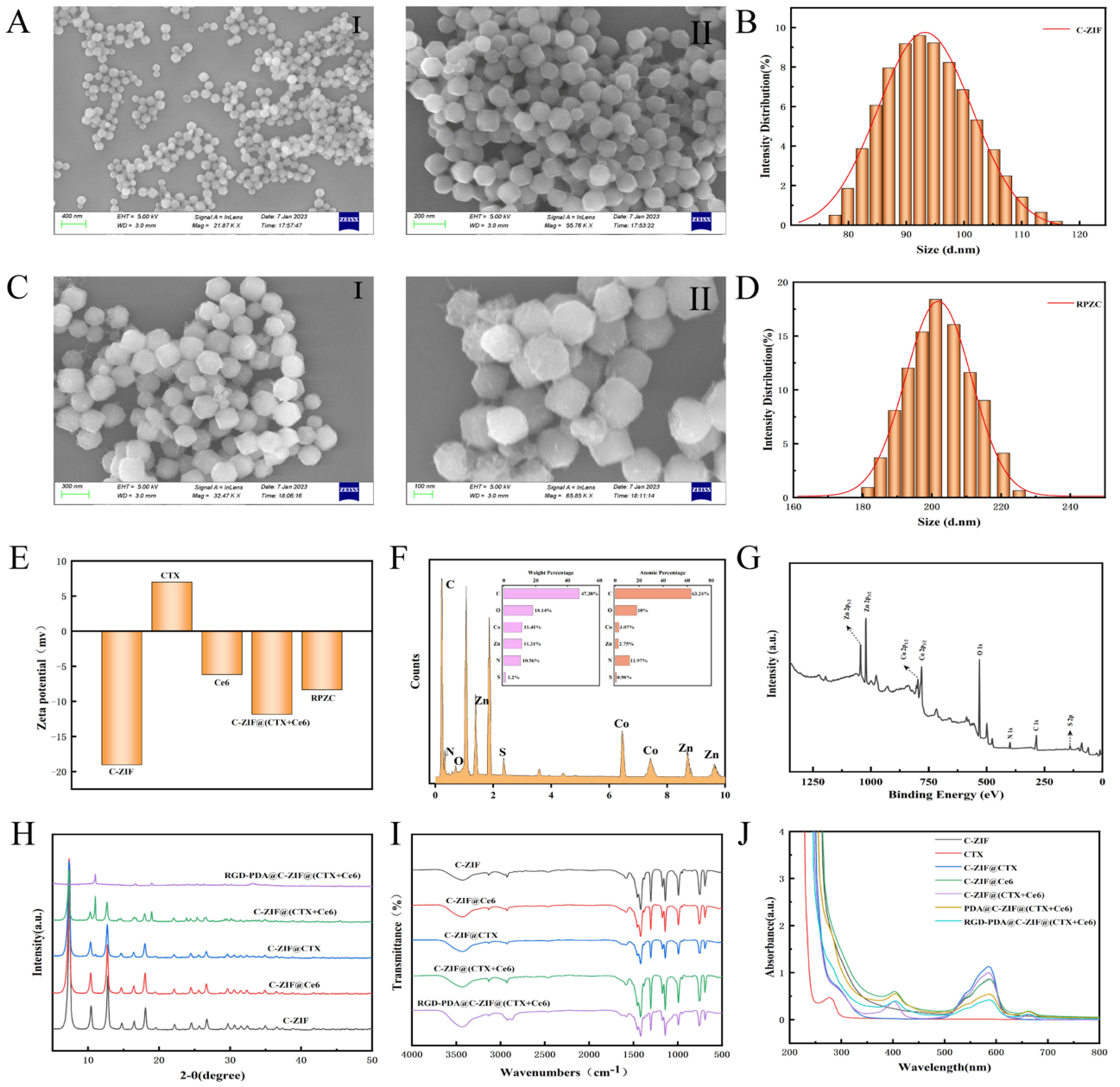

Figure 1 Characterization of RZCP:(**A**) SEM image of C-ZIF(**I, II**). (**B**) Size distributions of C-ZIF. (**C**) SEM image of RZCP (**I, II**). (**D**) Size distributions of RZCP. (**E**) Zeta-potentials at different synthetic steps. (**F**) Energy dispersive spectroscopy (EDS) of RZCP. (**G**) XPS spectrum of RZCP. (**H**) XRD of the different modified C-ZIF. (**I**) FT-IR spectra of the different modified C-ZIF. (**J**)UV−vis spectra of RZCP at different synthetic steps. (**B**, D, E and J created using Origin 2021 software).

(BET) method determined C-ZIF's specific surface area to be 1797.04 m²/g, with a pore diameter averaging 3.4344 nm (Figure S1, Supporting Information). The nitrogen adsorption isotherm revealed a significant specific surface area and pore diameter for C-ZIF, indicating its potential for drug-loading applications. After subsequent modification with PDA and RGD, the RGD-PDA@C-ZIF@(CTX+Ce6) took on a smoother and more rounded morphology (Figure 1C(I–II)) with an increased average size of about 201.87±2.49nm (Figure 1D). To further investigate the physicochemical properties of the nanocarrier platform, the Zeta potentials of C-ZIF, CTX, Ce6, C-ZIF@(CTX+Ce6), and RPZC were measured. As depicted in Figure 1E, upon loading CTX and Ce6 into C-ZIF, the nanoparticle's Zeta potential shifted from −19.04 mV to −11.88 Mv. Post further modifications, RPZC's Zeta potential rose to −8.33 mV. The alteration in Zeta potential suggests the successful loading of the positively charged CTX. Energy-dispersive X-ray spectroscopy (EDS) analysis of RPZC further corroborated its elemental composition, confirming the presence of representative

elements like Zn, Co, C, N, O, and S (Figure 1F). X-ray photoelectron spectroscopy (XPS) illuminated the surface chemical composition of the RPZC nanomaterial (Figure 1G; Figure S2, Supporting Information). Multiple oxidation states were evident, including Metal-O, C-O, and C=O, with their peaks at 530.04 eV, 531.26 eV, and 532.69 eV respectively. Comprehensive analysis revealed the primary elemental XPS peaks and their relative percentages. X-ray diffraction patterns (Figure 1H) showcased that, upon loading CTX and Ce6, C-ZIF retained its sharp characteristic peaks, affirming its crystalline structure's stability. However, after polydopamine encapsulation, the crystallinity of nanoparticles was altered, evidenced by the disappearance of sharp edges and attesting to the successful surface modification. Additionally, infrared spectra supported RPZC synthesis (Figure 1I), especially noting the presence of amine-thiol linkage disulfide functional groups at 2872.34 cm^{-1}. Ultraviolet absorption tests (Figure 1J) manifested characteristic absorption peaks for CTX and Ce6 at 277 nm and 404 nm respectively, further substantiating the successful synthesis of RPZC. The fluorescence intensity of RPZC, as detected by a fluorescence spectrophotometer, demonstrated an increase in absorbance with rising RPZC concentration (Figure S3, Supporting Information). Cumulatively, these results provide a comprehensive portrayal of RPZC's structure, chemical composition, and surface characteristics.

Detection of Oxygen Production

In the analysis of oxygen production, we assessed the dissolved oxygen content of C-ZIF and RPZC under identical conditions. Throughout the experiment, the concentration of dissolved oxygen was recorded at one-minute intervals, as depicted in Figure 2A and B. Under consistent experimental parameters, both C-ZIF and RPZC exhibited a gradual rise in oxygen yield, eventually plateauing. Notably, at the same concentration, C-ZIF demonstrated a superior yield compared to RPZC. To elucidate, after 15 minutes of sustained reaction, the dissolved oxygen content of 90μg/mL C-ZIF reached 19.9 mg/L, while the RPZC of equivalent concentration stood at 15.4 mg/L. This disparity arises due to RPZC's external layer, which is ensheathed in polydopamine, while, in contrast, C-ZIF possesses an abundance of Co^{2+} exposed to hydrogen peroxide, facilitating a more efficient decomposition of hydrogen peroxide into oxygen during the catalytic process. Consequently, the overall oxygen yield of RPZC is inferior to that of C-ZIF. These findings underscore RPZC's exemplary capability to catalyze the generation of oxygen from hydrogen peroxide. Such exceptional oxygen-producing prowess is paramount for photodynamic therapy. In tumor treatments, photodynamic therapy hinges on photosensitizers generating reactive oxygen, which subsequently inflicts damage and induces apoptosis in tumor cells.

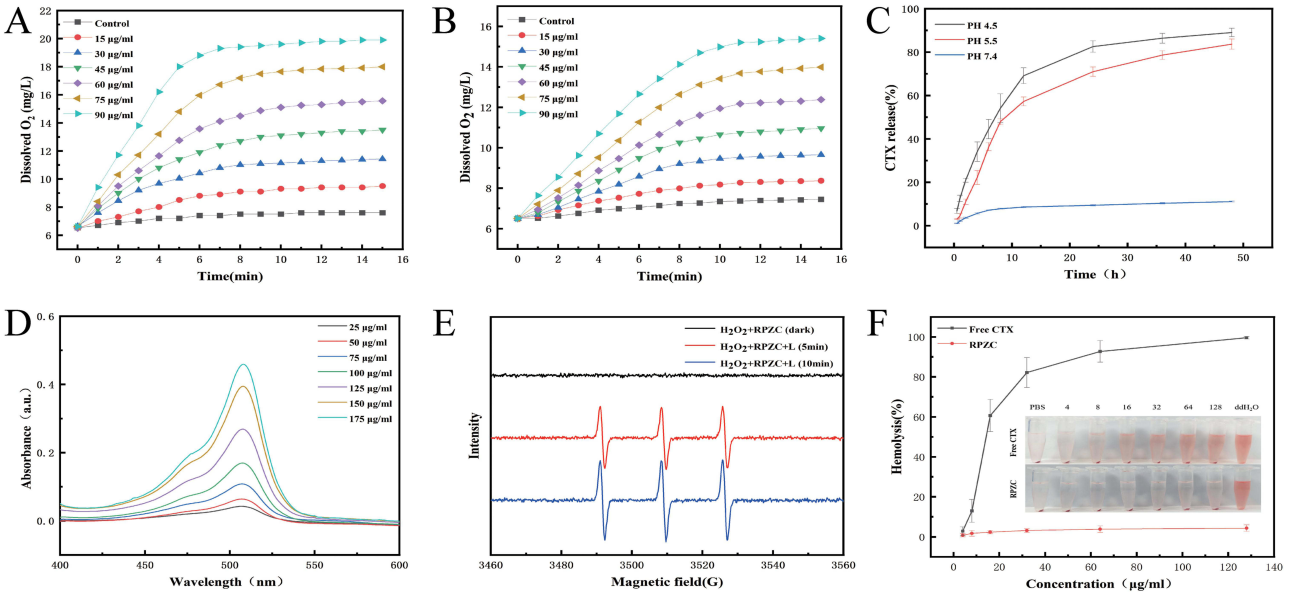

Figure 2 (**A**) Oxygen production of C-ZIF. (**B**) Oxygen production of RPZC. (**C**) CTX release process of RPZC at different pH. (**D**) SOSG probe detects the UV–vis spectra of $^1O_2$ generated by RZCP under 660nm laser irradiation. (**E**) ESR spectra of DMPO/$^1O_2$ collected from H_2O_2 with RPZC solution. (**F**) Conducted hemolysis assays on free CTX and RPZC at different concentrations, determining the relative hemolysis percentages. (**A**–**F** created using Origin 2021 software).

However, the localized oxygen levels within tumors are typically diminished, thereby curtailing the efficacy of photodynamic therapy. The Co^{2+} released by RPZC in the acidic tumor microenvironment possesses commendable oxygen-producing attributes, adeptly catalyzing the transformation of hydrogen peroxide into oxygen within the tumor milieu. This ameliorates the hypoxic conditions inherent to tumors, augmenting the therapeutic outcomes of photodynamic therapy and potentially mitigating the treatment resistance induced by tumor hypoxia.

CTX Release

Zn/Co ZIF is synthesized from organic linkers, 2-methylimidazole, and metal ions, namely zinc and cobalt. Within an acidic tumor microenvironment, the coordination between them dissociates, leading to the degradation of the framework and subsequent drug release.[25] Scanning electron microscopy delineates the morphological alterations of RPZC in acidic PBS with pH levels of 4.5 and 5.5, as illustrated in Figure S4 (Supporting Information). Within the acidic PBS solution, the RPZC structure undergoes pronounced disintegration. Utilizing the standard BCA protein quantification technique, the CTX loading and encapsulation efficiency for RPZC were determined to be 6.9wt% and 25.5%. CTX's in vitro release experiment in PBS solutions of varying pH levels, depicted in Figure 2C, reveals a markedly sluggish drug release rate for RPZC in PBS at pH 7.4; post 48 hours, only 11.11% of CTX is released. However, in the acidic PBS with pH levels of 4.5 and 5.5, CTX exhibited rapid release rates of 89.02% and 83.64%, respectively.

Measurement of Singlet Oxygen

Using the SOSG probe, we examined the ability of RPZC to generate singlet oxygen ($^1O_2$). Under illumination with a 660 nm laser, RPZC displayed a prominent absorption peak at 504 nm when in the presence of hydrogen peroxide (Figure 2D). The intensity of this peak increased proportionally with the concentration of RPZC, highlighting its potent capacity to produce $^1O_2$ under photonic excitation. To further corroborate the singlet oxygen generation by RPZC, we employed dimethyl pyridine N-oxide (DMPO) as a trapping agent for DMPO/$^1O_2$, which was subsequently recorded via electron spin resonance (ESR) spectroscopy (Figure 2E). In the absence of illumination, no corresponding signals were detected. However, as the exposure duration extended, the spectral intensity escalated, indicating the progressive decomposition of RPZC, thereby catalyzing enhanced oxygen generation. Consequently, under the irradiation of the 660 nm laser, the production of singlet oxygen by Ce6 surged.

Hemolysis Activity Assessment

Hemolytic toxicity is a pivotal criterion for evaluating the safety of biomaterials. At an RPZC concentration of 128μg/mL, hemolysis was a mere 4.33%. Notably, at this juncture, the CTX concentration surged to 16.64μg/mL. In contrast, when the free CTX concentration stood at 8μg/mL, the erythrocyte hemolysis rate reached 12.96% (Figure 2F). This underscores that our established nanoplatform can markedly mitigate the hemolytic activity of CTX, reducing its nonspecific cytotoxicity.

Targeting and Cytotoxicity of RPZC

To corroborate the in vitro cellular targeting capability of RPZC, HepG2 and THLE-2 cells were co-incubated with RPZC. Utilizing confocal laser scanning microscopy, we discerned that HepG2 cells subjected to RPZC exhibited pronounced red fluorescence, whereas no such fluorescence was apparent in THLE-2 cells (Figure 3A). This elucidates RPZC's commendable specificity to HepG2 cells and its subdued affinity for normal liver cells. RGD, a distinctive peptide sequence, exhibits an affinity for tumor cell surfaces that overexpress αvβ3 integrins.[26,27] Given the elevated expression of these integrins in HepG2 cells, RPZC, via RGD, binds to the cell's αvβ3 integrin surface, achieving targeted action. In contrast, regular liver cells, having a diminished αvβ3 integrin expression, do not facilitate stable binding with RPZC, hence the absence of significant red fluorescence in THLE-2 cells. These findings reinforce RPZC's targeted prowess in in vitro cell experiments. Target specificity is an indispensable characteristic of nanodrugs in oncology, enhancing the drug's selective action, reducing cytotoxicity to healthy cells, thereby amplifying therapeutic outcomes and diminishing side effects. To delve deeper into the uptake dynamics of HepG2 cells towards RPZC, they were treated with RPZC (100μg/mL) over varying durations. A mere 30-minute exposure showed negligible red

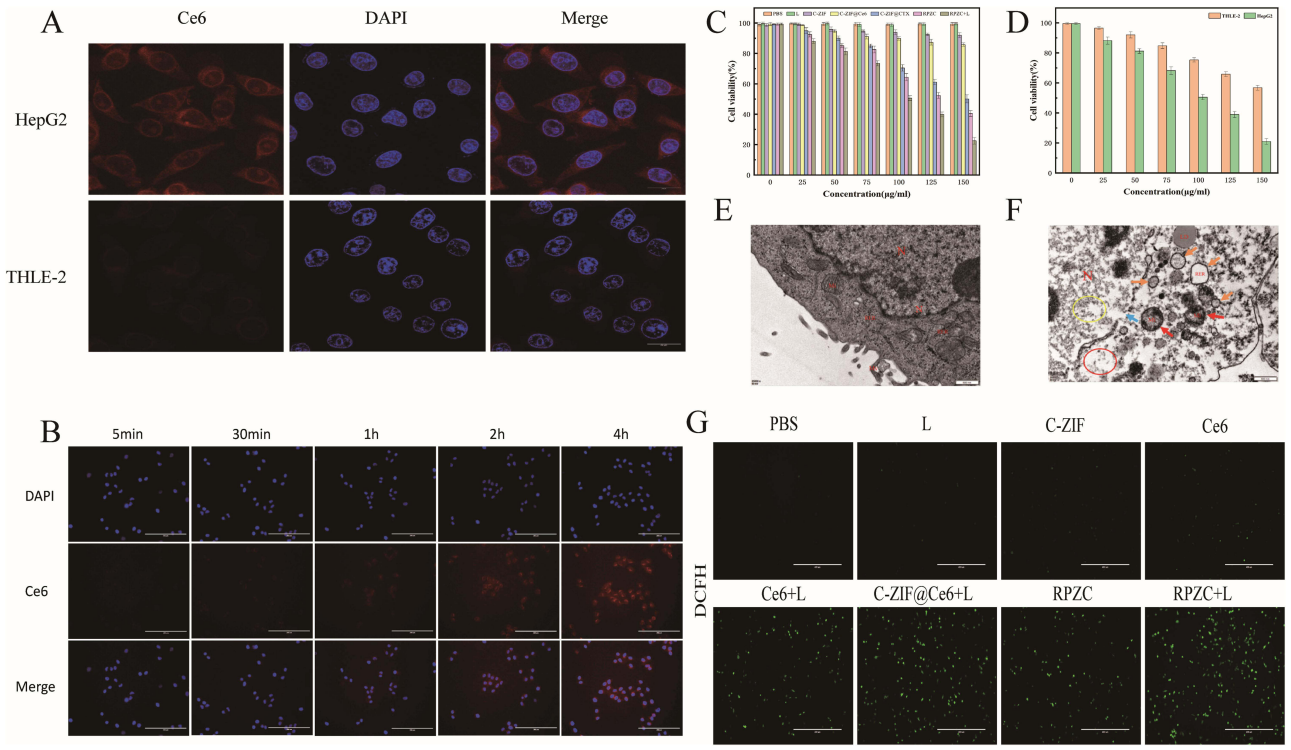

Figure 3 (**A**) Targeted analysis of RZCP to HepG$_2$ cell (Scale bar: 20 μm). (**B**) Fluorescence Microscope images of released Ce6 at different time that incubated with RZCP (100 μg/mL, Scale bar: 200 μm). (**C**) Cell viability of HepG2 cells that incubated with different concentration with different treatment (incubate for 24 hours). (**D**) Relative viabilities of HepG2 and THLE-2 cells treated with RPZC NPs +660nm Laser at different concentration. (**E** and **F**) TEM images demonstrating intracellular uptake after incubation with PBS and RPZC NPs+660nm Laser (Scale bar:500nm). (**G**) Fluorescence Microscope images of ROS generation that HepG2 cells incubated with different material (C-ZIF, Ce6, RPZC NPs) with or without laser (Scale bar: 400 μm). (**C** and **D** created using Origin 2021 software).

fluorescence from Ce6. As incubation persisted, the intensity of the Ce6 red fluorescence grew exponentially, culminating around the cell nucleus (Figure 3B), signifying that the engineered RPZC targets hepatocarcinoma cells, releasing Ce6 in a temporally dependent manner.

We investigated the effects of RPZC on cellular viability using the CCK-8 assay. As illustrated in Figure 3C, cells treated with PBS and subjected to 660nm laser irradiation remained unharmed. The influence of low concentrations of C-ZIF on cellular vitality was negligible. Even when C-ZIF concentration escalated to 150μg/mL, the viability of HepG2 cells remained above 90%. With increasing concentrations of the nanomaterial, cells exhibited varying degrees of toxicity when treated with C-ZIF@CTX and C-ZIF@Ce6 + 660nm laser. Compared to cells treated with RPZC without light exposure, those exposed to RPZC with light exhibited the most pronounced lethality. Concurrently, we assessed the cytotoxic effects of RPZC on both THLE-2 and HepG2 cells under identical treatment conditions. The findings demonstrated that under 660nm laser irradiation, the vitality of both cell types diminished with rising RPZC concentrations. Notably, the cytotoxic effect of RPZC on HepG2 was significantly more potent than on THLE-2 cells (Figure 3D); at a RPZC concentration of 150μg/mL, HepG2 cell viability was a mere 20%, whereas THLE-2 cells retained a vitality over 50%. This differential effect can be attributed to the RGD modifications on the surface of RPZC, conferring active targeting to liver cancer cells. Transmission electron microscopy revealed ultrastructural alterations in cells post RPZC with light treatment. As depicted in Figure 3E, post-PBS treated HepG2 cells exhibited evenly distributed chromatin, predominantly euchromatin, with distinct nucleoli and intact nuclear membranes. Organelles were clearly delineated, and the cell membrane was continuous, displaying sparse elongated microvilli. However, in contrast to the normative HepG2 cells, those treated with RPZC+Laser displayed irregular nuclei, significant chromatin loss, and ruptured nuclear membranes. Mitochondria appeared swollen, while the rough endoplasmic reticulum expanded into a spherical shape. There was a substantial loss of cytoplasmic content, and the cell membrane was compromised (Figure 3F).

It is well-established that the efficacy of PDT (Photodynamic Therapy) hinges largely upon the generation of ROS, which possess the capacity to eradicate tumor cells. To gauge the level of ROS produced by RPZC under external laser irradiation, we employed the quintessential ROS probe, DCFH-DA, and corroborated our findings via fluorescence microscopic imaging. As delineated in Figure 3G, in comparison to the control group, cells subjected to free Ce6 and 660 nm light exposure manifested a faint green fluorescent signal, attributed to the poor water solubility of Ce6, resulting in minimal direct uptake by liver cancer cells. However, following treatment with C-ZIF@Ce6 and 660 nm illumination, there was a marked amplification in ROS generation. Intriguingly, the ultimate product, RPZC, when exposed to laser irradiation, displayed the most potent green fluorescence indicative of ROS across all groups, suggesting an elevated ROS generation within liver cancer cells by RPZC. This can be ascribed to the active targeting facilitated by the RGD modification on RPZC's surface, enabling hepatoma cells to assimilate an augmented quantity of Ce6, which in turn, under 660 nm laser exposure, spawns an increased amount of singlet oxygen.

Evaluation of Antitumor Effect of RPZC in vitro

Tumor metastasis is a critical phase in the progression of liver cancer, often leading to treatment failure and disease recurrence. Understanding the molecular mechanisms behind metastasis is crucial for devising effective treatment strategies, with processes such as epithelial-to-mesenchymal transition (EMT) playing an important role in cancer metastasis.[28] This metastatic cascade facilitates the dissemination and invasion of liver cancer, contributing significantly to therapeutic failures.[29] The scratch assay, routinely employed to study cellular migratory capabilities, assesses the rate and modality by which cells migrate and fill the scratched area, providing insights into the mechanisms and regulation of cell movement. As illustrated in Figure 4A, following interventions with PBS, laser irradiation, and unmodified C-ZIF, the cellular scratches were predominantly healed by the 48-hour mark, indicating that these treatments did not perturb HepG2 cell migration. Conversely, the group subjected to RPZC coupled with laser irradiation exhibited a pronounced inhibition in wound closure. Therefore, the combination of RPZC with laser irradiation can inhibit the migration of HepG2 cells, providing a potential strategy for preventing liver cancer metastasis.

The mitochondrial membrane potential signifies the voltage differential across the inner mitochondrial membrane, standing as a quintessential factor in upholding mitochondrial functionality and energy production. It plays an instrumental role in cellular metabolism, survival, and apoptotic pathways.[30] The JC-1 stain is utilized to observe alterations in the mitochondrial membrane potential post various treatments. As depicted in Figure 4B, there was no discernible difference in the intensity of the red fluorescence signal among the PBS, laser-irradiated, and C-ZIF treated groups, indicating that these interventions elicited negligible shifts in the cellular mitochondrial potential. In the C-ZIF@Ce6, C-ZIF@Ce6+laser, and C-ZIF@CTX groups, there was a progressive attenuation of the red fluorescence signal, concomitant with an augmentation of the green fluorescence. This suggests that under photoinduction, the C-ZIF nanoparticles gradually disintegrate, releasing Ce6 and CTX, which in turn perturb the cell's mitochondrial potential and instigate apoptosis. Most notably, in the RPZC combined with light exposure group, we observed a pronounced decrease in the red fluorescence and a surge in the green fluorescence. This implies that, under photostimulation, RPZC nanoparticles, through the release of Ce6 and CTX, bolster ROS generation and cytotoxic effects, orchestrating a synergistic assault against hepatocellular carcinoma, markedly altering the cell's mitochondrial membrane potential, culminating in elevated apoptotic events.

Utilizing Calcein/PI staining, we have assessed viable and deceased cells. As illustrated in Figure 4C, cells treated with PBS, subjected to laser irradiation, and those in the C-ZIF group predominantly exhibited green fluorescence, indicating an absence of cellular apoptosis. Conversely, in the cells treated with C-ZIF@Ce6, C-ZIF@Ce6 with phototherapy, and C-ZIF@CTX, there was a discernible integration of increasing red fluorescence within the green glow. Cells exclusively treated with RPZC displayed a heightened presence of red fluorescence, potentially attributable to the targeted action of RGD, leading to augmented cellular uptake of CTX. Post exposure to 660 nm laser illumination, the proportion of red fluorescence in the RPZC-treated cells significantly escalated, evidencing the synergistic interplay of RPZC's cytotoxic and photodynamic effects, culminating in the apoptosis of liver cancer cells.

Subsequently, we delved into its synergistic therapeutic action through in vitro apoptosis assays. As anticipated, phototherapy in conjunction with RPZC triggered a substantial 66.75% of cellular apoptosis/necrosis. In contrast,

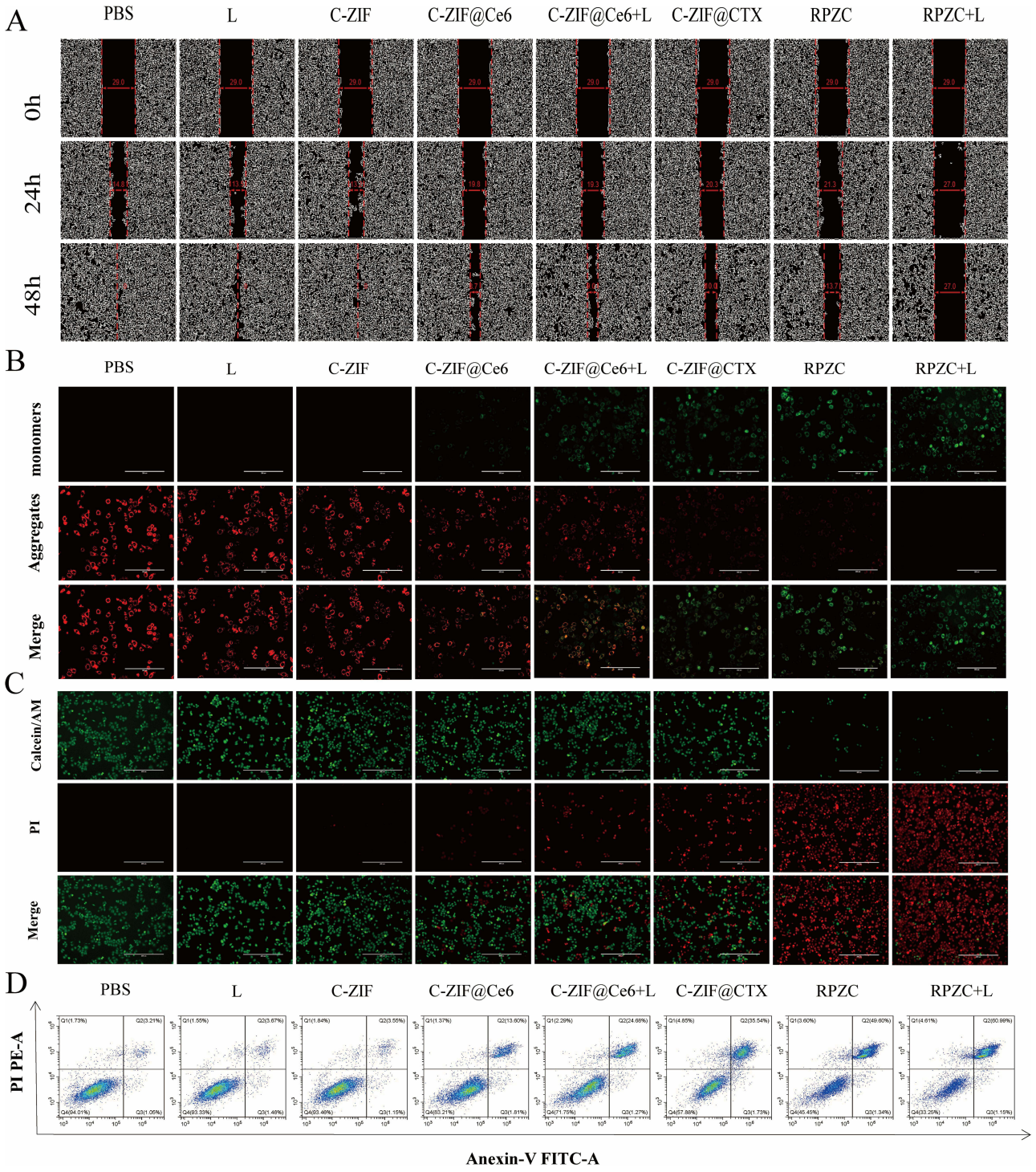

Figure 4 (**A**) Microscopy images obtained in the wound healing experiment that incubated with different treatment (PBS, 660 nm Laser, C-ZIF, C-ZIF@Ce6, C-ZIF@Ce6 +660 nm Laser, C-ZIF@CTX, RZCP NPs and RZCP NPs+660 nm Laser). (**B**) JC-1 staining on HepG2 cells that incubated with different materials (Scale bar: 200 μm). (**C**) Calcein-AM/PI dual staining images of HepG2 cells that incubated with different materials with or without laser irradiation(Scale bar: 400 μm). (**D**) Flow cytometry images of HepG2 cells that treated with different materials by Annexin V-FITC/PI test kit.

C-ZIF@Ce6 with phototherapy and C-ZIF@CTX instigated 28.25% and 42.12% apoptosis/necrosis respectively (Figure 4D). These findings accentuate the pronounced deleterious impact of the combined therapy on HepG2 cells, where leveraging CTX and Ce6 on C-ZIF manifested superior therapeutic outcomes compared to singular cytotoxic or

photodynamic interventions. The in vitro cytotoxicity assay results underscore that amalgamating cytotoxic agents with photodynamic therapy can profoundly amplify the anti-tumor efficacy.

Multimodal Imaging

Upon administering nanoparticles (200 μL, 150 μg/mL) via tail vein injection into tumor-bearing mice, we scrutinized the fluorescence intensity at the tumor site over various time intervals. As depicted in Figure 5A, post-RPZC injection, a discernible fluorescence signal commenced around the 4th hour at the tumor locale, culminating in its zenith by the 6th hour. Subsequently, this luminescence tapered off over time. In contrast, non-RGD modified nanoparticles exhibited negligible fluorescence accumulation at the tumor site. RPZC, acting as a targeted drug-delivery platform, demonstrates pivotal in vivo targeting capabilities. RGD peptide modification enables RPZC to precisely home in on the tumor site. We observed a conspicuous fluorescence in tumor tissues treated with RPZC, attributed to the RGD's targeting functionality, thereby facilitating nanoparticle accumulation around tumor cells, resulting in enhanced luminescence. Conversely, non-RGD modified nanoparticles, bereft of specific targeting, exhibited scant accumulation and muted fluorescence. Ex vivo imaging of tumor tissues and primary organs at the 6th hour (Figure 5B–D) elucidated RPZC's in vivo distribution. Compared to the PZC group, the fluorescence intensity in the RPZC group's tumor tissues is significantly higher ($P < 0.01$), indicating the effective enrichment of RPZC at the tumor site. This data fortifies RPZC's stellar targeting capabilities, enabling effective tumor-targeted imaging in vivo. To evaluate the magnetic resonance response signal in tumor tissues of nude mice, RPZC (200 μL, 150 μg/mL) was administered via tail vein injection at different intervals. A 4-hour post-injection, a surge in brightness was discerned at the tumor site, peaking at the 6th hour (Figure 5E). Our findings underscore RPZC's superior in vivo targeting attributes, achieving substantial fluorescence/magnetic resonance signal accumulation at the tumor site, thereby bolstering precision tumor imaging. Observing these temporal signal

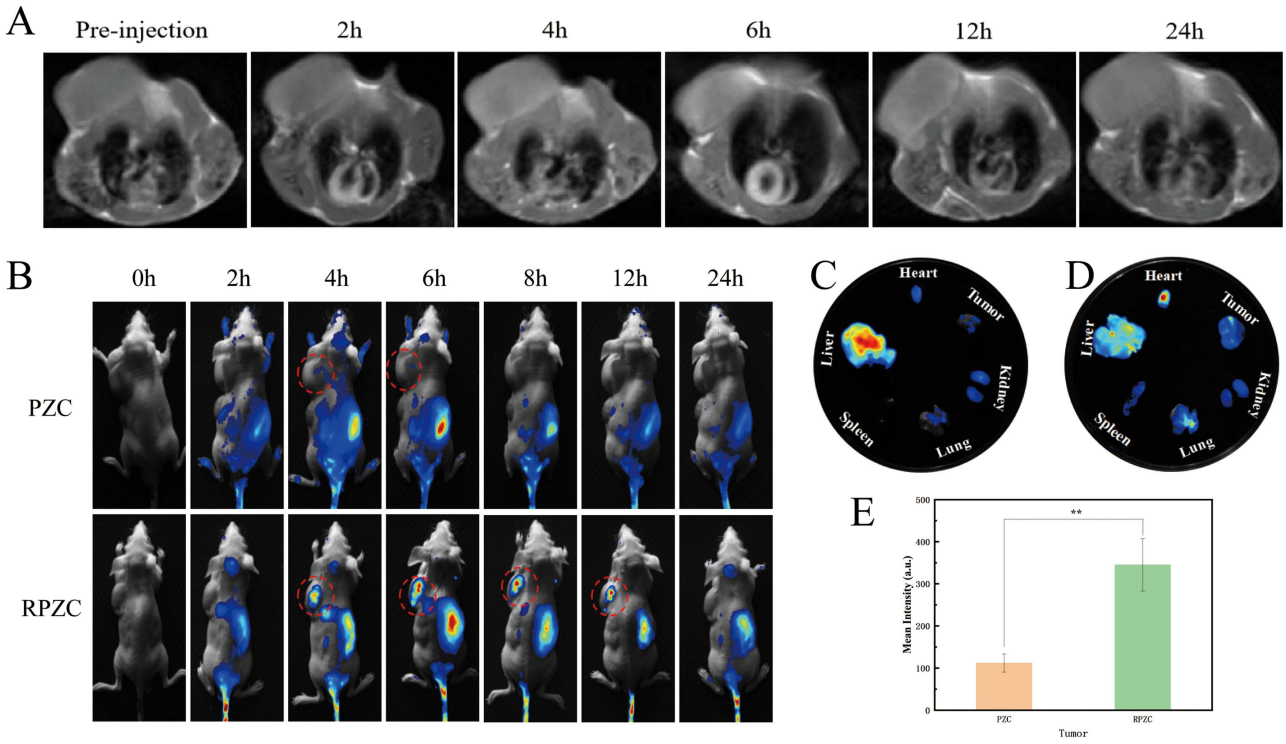

Figure 5 (**A**) In vivo MRI images of HepG2 tumor-bearing mice after tail vein injection of RPZC at different times. (**B**) In vivo fluorescence images of HepG2 tumor-bearing mice after tail vein injection of PZC and RPZC at different times. The red circles indicated the tumor sites. (**C**) In vitro fluorescence images of major mouse organs and tumors at 6h after injection of RPZC. (**D**) In vitro fluorescence images of major mouse organs and tumors at 6h after injection of PZC. (**E**) Fluorescence intensities of major mouse organs and tumors as evaluated by quantitative analysis. (**E** was created using Origin 2021 software. n = 3. Statistical analysis was conducted using a *t*-test. *$p < 0.05$, **$p < 0.01$).

variations further unveils the dynamic intracorporeal distribution and accumulation of nanoparticles, offering invaluable insights and guidance for their therapeutic application in tumor diagnostics and treatment.

Evaluation of Anti-Tumor Effects of RPZC in vivo

To investigate the in vivo antitumor efficacy of RPZC, experimental studies were conducted on tumor-bearing nude mice. These mice were arbitrarily segregated into eight groups (n=5): G1). PBS, G2) Laser, G3) C-ZIF, G4) C-ZIF@Ce6, G5) C-ZIF@Ce6+Laser, G6) C-ZIF@CTX, G7) RPZC, G8) RPZC+Laser. The treatment schematic is illustrated in Figure 6A.

Initially, we employed Inductively Coupled Plasma Mass Spectrometry (ICP-MS) to investigate the metabolism and clearance processes of RPZC in vivo. Utilizing cobalt as a tracer element, we ascertained the blood half-life of RPZC. As

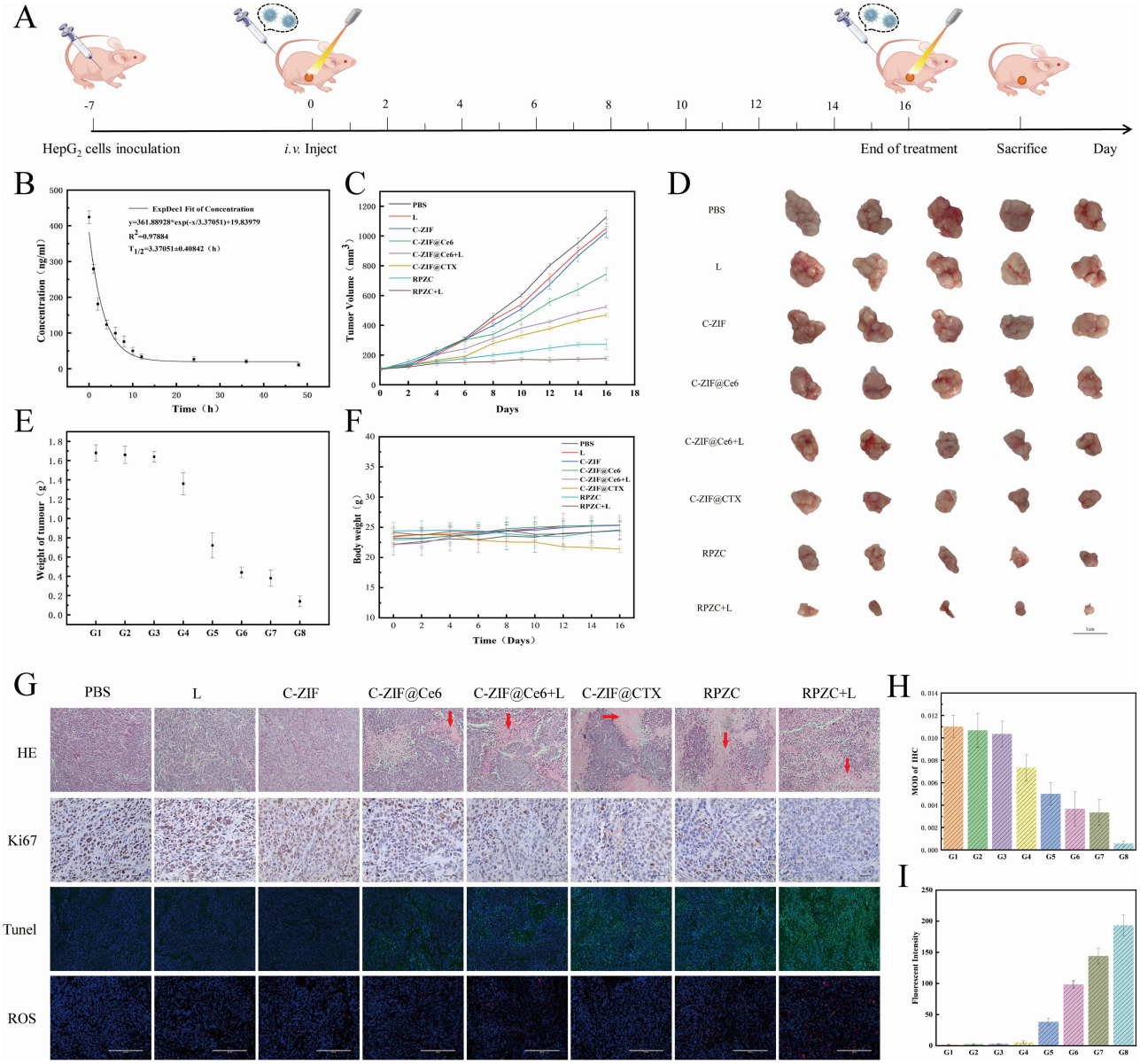

Figure 6 (**A**) Schematic illustration of the experimental approach of RPZC In vivo. (**B**) Pharmacokinetics profiles of RPZC after i.v. injection into the mice. (**C**) Growth curves of tumors with disparate treatments. (**D**) Representative tumor photographs of mice from each treatment group post-treatment (Scale bar: 1 cm). (**E**) The weights of tumors dissected from mice across different treatment groups (G1: PBS, G2:660 nm Laser, G3: C-ZIF, G4: C-ZIF@Ce6, G5: C-ZIF@Ce6+660 nm Laser, G6: C-ZIF@CTX, G7: RZCP NPs, G8: RZCP NPs+660 nm Laser). (**F**) Body weight variation with different treatment. (**G**) H&E, Ki-67, Tunel and ROS staining of tumor tissue from various treatment. (**H**) Quantification of Ki-67 expression. (**I**) Quantification of Tunel green fluorescence intensity. (**B**, **C**, **E**, **F**, **H**, **I** created using Origin 2021 software).

illustrated in Figure 6B, the blood half-life of RPZC stands at 3.37±0.41h. This can likely be attributed to its optimal size (approximately 200 nm), which proficiently circumvents rapid clearance by the liver and kidneys. Moreover, the presence of polydopamine on the RPZC surface may facilitate the nanoparticles in evading swift phagocytosis by macrophages, thereby prolonging its circulation time. Such an evasion mechanism potentially aids RPZC in sustaining an extended blood half-life, enhancing its in vivo stability and pharmacokinetic properties.

Upon concluding the treatment regimen, tumors from each group were dissected as depicted in Figure 6C–E. Tumors from the PBS, phototherapy, and C-ZIF groups showed no signs of growth inhibition, with their volumes persistently expanding. In line with our in vitro findings, tumors treated with C-ZIF@Ce6, C-ZIF@Ce6+Laser, and C-ZIF@CTX began to exhibit discernible antitumor effects, presumably due to the singular photodynamic therapy and cytotoxic effects. RPZC-treated tumors exhibited a slower growth, attributed to RGD-mediated active targeting and the Enhanced Permeability and Retention (EPR) effect, allowing RPZC to significantly accumulate within the tumor sites. Consequently, the cytotoxic release of CTX within the tumor milieu leads to the eradication of cancer cells. Compared to the RPZC group, the RPZC+Laser group manifested a more pronounced antitumor effect, potentially due to the augmented photodynamic therapy effect of RPZC on the tumor cells. Simultaneously, CTX accumulation at the tumor site drastically eradicated cancer cells, with the combined therapeutic strategies markedly enhancing efficacy. In vivo findings underscored RPZC's pronounced combined cytotoxic and photodynamic therapeutic implications. When assessing the weight of mice across groups, with the exception of the C-ZIF@CTX group displaying a decline, no significant variances were observed (Figure 6F). We postulate that this might be due to the absence of polydopamine encapsulation on the C-ZIF@CTX material's surface, causing partial CTX leakage from ZIF pores during transportation, thus eliciting non-specific cytotoxic effects on the organism.

H&E staining, Ki67, TUNEL, and ROS were utilized for histopathological evaluations of tumor tissues. As indicated in Figure 6G–I, almost no apoptotic cells were observed in tumors from the PBS, Laser, and C-ZIF groups. In stark contrast, the RPZC+Laser group exhibited a significantly higher proportion of apoptotic cells compared to other groups. Immunohistochemical findings revealed a high Ki67 expression in the PBS, Laser, and C-ZIF groups, signifying unimpeded hepatocarcinoma proliferation. Conversely, a subsequent decline in Ki67 expression was noted in later groups, with the lowest expression found in the RPZC+Laser group, indicating significant inhibition of hepatocarcinoma proliferation, a finding consistent with our tumor volume observations.

Reactive oxygen species within tumor tissues were assessed using a ROS probe. With phototherapy, a faint red fluorescence was discerned upon treating the tumor with C-ZIF@Ce6, while a pronounced red fluorescence signal was evident in the RPZC group. This suggests that the Ce6 in RPZC was effectively taken up by the hepatocarcinoma tissue. Co^{2+} catalyzed the generation of oxygen from hydrogen peroxide, resulting in the production of reactive oxygen species with anti-tumor effects upon external phototherapy. Findings highlighted that the RPZC+Laser treatment induced the highest level of necrosis in hepatocarcinoma tissues.

Major organs (heart, liver, spleen, lungs, and kidneys) were stained with H&E as shown in Figure 7A, revealing no discernible damage across all organs. Hematological parameters for mice across all eight treatment groups, including red blood cell count, white blood cell count, hemoglobin concentration, platelet count, Alanine Aminotransferase (ALT), and Aspartate Aminotransferase (AST) remained within normal parameters (Figure 7B–G). These insights attest to the commendable biocompatibility of our devised RPZC nanoreactor, suggesting negligible or no detrimental side-effects on major organs.

Conclusion

In this study, we have developed a multifunctional nanomaterial, RPZC, which combines cytotoxin and photodynamic therapy for the treatment of liver cancer. Our research focused on the design, preparation, and application of the RPZC nanoreactor, exploring its effects and potential in treating liver cancer. Through a series of in vitro and in vivo experiments, we systematically have assessed the drug delivery, cytotoxicity, and photodynamic therapeutic effects of RPZC, uncovering its mechanisms of action at cellular and tissue levels. As an innovative nanomedicine platform, RPZC efficiently loaded both cytotoxins and photosensitizers, demonstrating remarkable anti-tumor efficacy in vitro by inhibiting the growth and migration of liver cancer cells. Pharmacokinetic studies in vivo revealed RPZC's commendable blood half-life and circulatory stability,

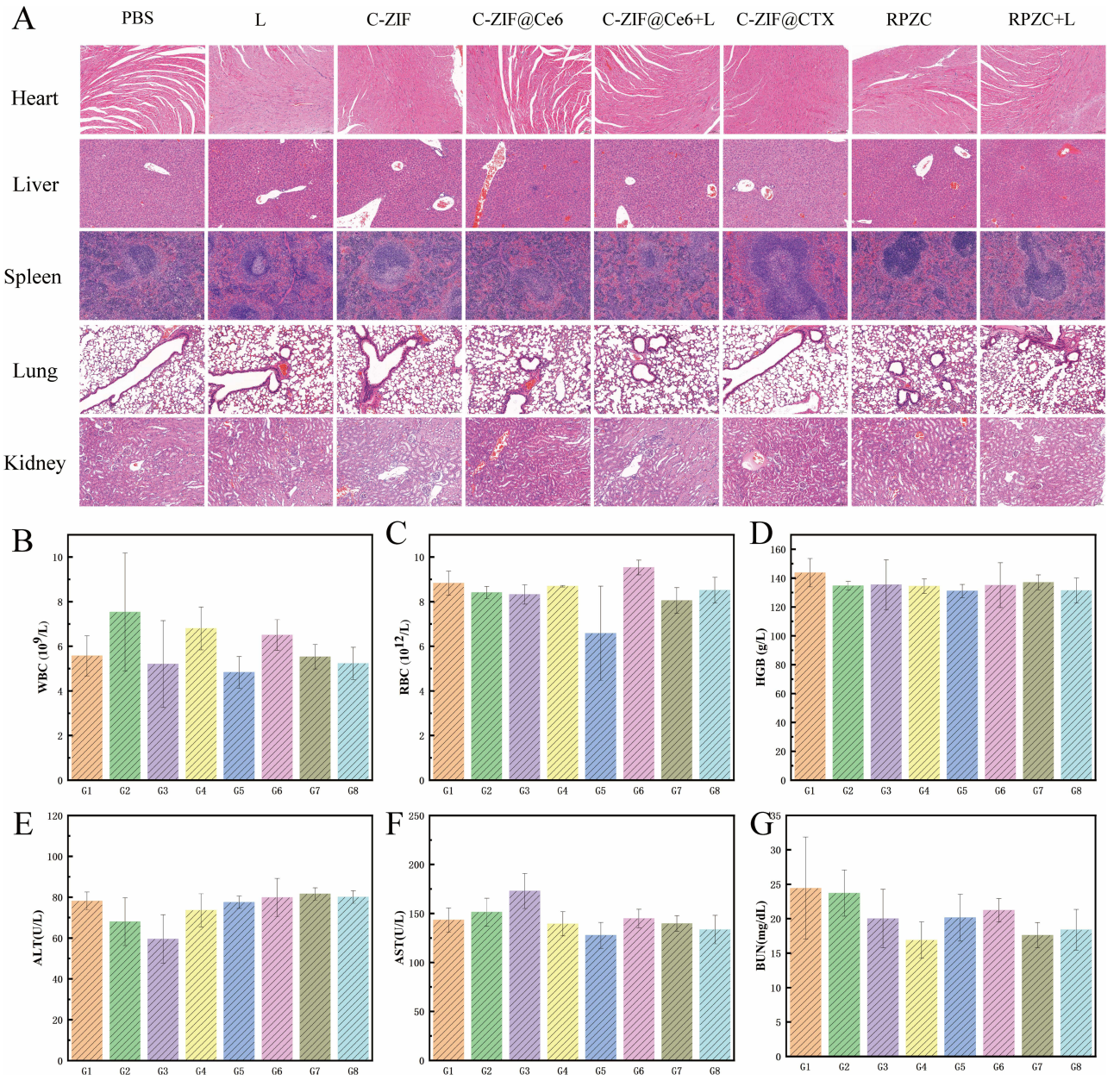

Figure 7 (**A**) H&E staining of major organs in mice with various treatments(Scale bar:100μm). (**B**–**G**) Hemanalysis of WBC count, RBC count, HGB, ALT, AST, and BUN. (**B**–**G** created using Origin 2021 software). Data are presented as the mean ± SEM (n = 3).

supporting its potential for sustained drug delivery. Using multimodal imaging techniques, we authenticated RPZC's tumor-targeting ability, facilitated by the modified RGD peptide, which enabled precise tumor site accumulation, offering new avenues for early tumor detection and analysis, laying a firm groundwork for precision medicine. Importantly, RPZC demonstrated a significant advantage in combined cytotoxicity and photodynamic therapy, efficiently accumulating at tumor sites and inducing substantial apoptosis upon photodynamic stimulation in vivo. This combined treatment not only enhanced the toxic effect on tumor cells but also laid a foundation for consistent therapeutic outcomes.

However, it is pivotal to acknowledge that, despite the substantial findings of our study, further research and validation remain essential. For instance, an in-depth examination of the toxicity, metabolic pathways, biodegradability of the RPZC nanoreactor, and more intricate in vivo experimental verifications represent crucial future research directions. Furthermore, considering different tumor types and individual variances, a more exhaustive study on the therapeutic efficacy and safety of RPZC nanoreactor is imperative.

In conclusion, this study introduces an innovative nano-therapeutic strategy for liver cancer treatment and contributes significantly to the fields of nanomedicine and precision therapy. While challenges and queries remain, we believe that with the advancement of science and technology, RPZC holds promise for delivering more effective and reliable solutions for malignant tumors like liver cancer.

Ethics Approval and Consent to Participate

This study was conducted in accordance with the guidelines of the Ministry of Science and Technology of China and relevant national regulations, and was approved by the Ethics Committee of the Second Affiliated Hospital of Guangxi Medical University (Approval Number: 2023-KY (0910)).

Acknowledgments

This work was supported by the Natural Science Foundation of Guangxi (Grant Number 2022GXNSFAA035459) and the Guangxi Snake Research Association [2023] KT-06.

Disclosure

The authors declare no competing interests in this work.

References

1. Rumgay H, Arnold M, Ferlay J, et al. Global burden of primary liver cancer in 2020 and predictions to 2040. *J Hepatol*. 2022;77(6):1598–1606. doi:10.1016/j.jhep.2022.08.021
2. Chan LK, Tsui YM, Ho DW, Ng IO. Cellular heterogeneity and plasticity in liver cancer. *Semin Cancer Biol*. 2022;82:134–149. doi:10.1016/j.semcancer.2021.02.015
3. Ladd AD, Duarte S, Sahin I, Zarrinpar A. Mechanisms of drug resistance in HCC. *Hepatology*. 2024;79(4):926–940. doi:10.1097/HEP.0000000000000237
4. Chen R, Zhao C, Chen Z, et al. A bionic cellulose nanofiber-based nanocage wound dressing for NIR-triggered multiple synergistic therapy of tumors and infected wounds. *Biomaterials*. 2022;281:121330. doi:10.1016/j.biomaterials.2021.121330
5. Jeong H, Park W, Kim DH, Na K. Dynamic nanoassemblies of nanomaterials for cancer photomedicine. *Adv Drug Deliv Rev*. 2021;177:113954. doi:10.1016/j.addr.2021.113954
6. Li Z, Guo L, Lin L, et al. Porous SiO(2)-based reactor with self-supply of O(2) and H(2)O(2) for synergistic photo-thermal/photodynamic therapy. *Int J Nanomed*. 2023;18:3623–3639. doi:10.2147/IJN.S387505
7. Cui R, Shi J, Liu Z. Metal-organic framework-encapsulated nanoparticles for synergetic chemo/chemodynamic therapy with targeted H(2)O(2) self-supply. *Dalton Trans*. 2021;50(43):15870–15877. doi:10.1039/D1DT03110D
8. Kalita B, Utkin YN, Mukherjee AK. Current insights in the mechanisms of cobra venom cytotoxins and their complexes in inducing toxicity: implications in antivenom therapy. *Toxins*. 2022;14(12):839. doi:10.3390/toxins14120839
9. Chong HP, Tan KY, Tan CH. Cytotoxicity of snake venoms and cytotoxins from two southeast asian cobras (Naja sumatrana, Naja kaouthia): exploration of anticancer potential, selectivity, and cell death mechanism. *Front Mol Biosci*. 2020;7:583587. doi:10.3389/fmolb.2020.583587
10. Lafnoune A, Lee SY, Heo JY, et al. Anti-cancer effect of Moroccan cobra naja haje venom and its fractions against hepatocellular carcinoma in 3D cell culture. *Toxins*. 2021;13(6):402. doi:10.3390/toxins13060402
11. Derakhshani A, Silvestris N, Hajiasgharzadeh K, et al. Expression and characterization of a novel recombinant cytotoxin II from Naja naja oxiana venom: a potential treatment for breast cancer. *Int J Biol Macromol*. 2020;162:1283–1292. doi:10.1016/j.ijbiomac.2020.06.130
12. Al-Quraishy S, Dkhil MA, Abdel Moneim AE. Hepatotoxicity and oxidative stress induced by Naja haje crude venom. *J Venom Anim Toxins Incl Trop Dis*. 2014;20(1):42. doi:10.1186/1678-9199-20-42
13. Das T, Bhattacharya S, Halder B, et al. Cytotoxic and antioxidant property of a purified fraction (NN-32) of Indian Naja naja venom on Ehrlich ascites carcinoma in BALB/c mice. *Toxicon*. 2011;57(7–8):1065–1072. doi:10.1016/j.toxicon.2011.04.012
14. Li F, Shrivastava IH, Hanlon P, Dagda RK, Gasanoff ES. Molecular mechanism by which cobra venom cardiotoxins interact with the outer mitochondrial membrane. *Toxins*. 2020;12(7):425. doi:10.3390/toxins12070425
15. Attarde SS, Pandit SV. Anticancer potential of nanogold conjugated toxin GNP-NN-32 from Naja naja venom. *J Venom Anim Toxins Incl Trop Dis*. 2020;26:e20190047. doi:10.1590/1678-9199-jvatitd-2019-0047
16. Li X, Chen L, Huang M, et al. Innovative strategies for photodynamic therapy against hypoxic tumor. *Asian J Pharm Sci*. 2023;18(1):100775. doi:10.1016/j.ajps.2023.100775
17. Jo YU, Sim H, Lee CS, Kim KS, Na K. Solubilized chlorin e6-layered double hydroxide complex for anticancer photodynamic therapy. *Biomater Res*. 2022;26(1):23. doi:10.1186/s40824-022-00272-8
18. Maharjan PS, Bhattarai HK. Singlet oxygen, photodynamic therapy, and mechanisms of cancer cell death. *J Oncol*. 2022;2022:7211485. doi:10.1155/2022/7211485
19. Jiang W, Liang M, Lei Q, Li G, Wu S. The current status of photodynamic therapy in cancer treatment. *Cancers*. 2023;15(3):585. doi:10.3390/cancers15030585
20. Olszowy M, Nowak-Perlak M, Wozniak M. Current Strategies in Photodynamic Therapy (PDT) and Photodynamic Diagnostics (PDD) and the future potential of nanotechnology in cancer treatment. *Pharmaceutics*. 2023;15(6):1712. doi:10.3390/pharmaceutics15061712
21. Ur Rehman S, Sun M, Xu M, et al. Carbonized zeolitic imidazolate framework-67/polypyrrole: a magnetic-dielectric interface for enhanced microwave absorption properties. *J Colloid Interface Sci*. 2020;574:87–96. doi:10.1016/j.jcis.2020.04.053

22. Yang C, Tiwari SK, Guo L, et al. Zn-Co metal organic frameworks coated with chitosand and Au nanoparticles for chemo-photothermal-targeted combination therapy of liver cancer. *Front Oncol*. 2023;13:1110909. doi:10.3389/fonc.2023.1110909
23. George BP, Chota A, Sarbadhikary P, Abrahamse H. Fundamentals and applications of metal nanoparticle- enhanced singlet oxygen generation for improved cancer photodynamic therapy. *Front Chem*. 2022;10:964674. doi:10.3389/fchem.2022.964674
24. Ishiguro A, Nishioka M, Morishige A, et al. What is the best wavelength for the measurement of hemolysis index? *Clin Chim Acta*. 2020;510:15–20. doi:10.1016/j.cca.2020.06.046
25. Lv Y, Ding D, Zhuang Y, et al. Chromium-doped zinc gallogermanate@zeolitic imidazolate framework-8: a multifunctional nanoplatform for rechargeable in vivo persistent luminescence imaging and pH-responsive drug release. *ACS Appl Mater Interfaces*. 2019;11(2):1907–1916. doi:10.1021/acsami.8b19172
26. Paulus J, Nachtigall B, Meyer P, Sewald N. RGD peptidomimetic MMAE-conjugate addressing integrin αVβ3-expressing cells with high targeting index*. *Chemistry*. 2022;29(12):e202203476.
27. Li Y, Hu P, Wang X, Hou X, Liu F, Jiang X. Integrin αvβ3-targeted polydopamine-coated gold nanostars for photothermal ablation therapy of hepatocellular carcinoma. *Regen Biomater*. 2021;8(5):rbab046. doi:10.1093/rb/rbab046
28. Shi Y, Wang J, Huang G, et al. A novel epithelial-mesenchymal transition gene signature for the immune status and prognosis of hepatocellular carcinoma. *Hepatol Int*. 2022;16(4):906–917. doi:10.1007/s12072-022-10354-3
29. He Q, Lin Z, Wang Z, et al. SIX4 promotes hepatocellular carcinoma metastasis through upregulating YAP1 and c-MET. *Oncogene*. 2020;39 (50):7279–7295. doi:10.1038/s41388-020-01500-y
30. Popgeorgiev N, Gil C, Berthenet K, Bertolin G, Ichim G. Shedding light on mitochondrial outer-membrane permeabilization and membrane potential: state of the art methods and biosensors. *Semin Cell Dev Biol*. 2023;156:58–65. doi:10.1016/j.semcdb.2023.07.003